

Optical and X-ray analysis of the cluster of galaxies Abell 496. *

F. Durret^{1,2}, C. Adami^{3,4}, D. Gerbal^{1,2}, and V. Pislar^{1,5}

¹ Institut d'Astrophysique de Paris, CNRS, 98bis Bd Arago, F-75014 Paris, France

² DAEC, Observatoire de Paris, Université Paris VII, CNRS (UA 173), F-92195 Meudon Cedex, France

³ IGRAP, Laboratoire d'Astronomie Spatiale, Traverse du Siphon, F-13012 Marseille, France

⁴ Department of Physics and Astronomy, Northwestern University, Dearborn Observatory, 2131 Sheridan, 60208-2900 Evanston, USA

⁵ Université du Havre, 25 rue Philippe Lebon, 76600 Le Havre, France

Received 17 December 1999/ Accepted

Abstract. We present a detailed analysis of the cluster of galaxies Abell 496. The optical data include a redshift catalogue of 466 galaxies, out of which 274 belong to the main cluster and a CCD photometric catalogue in a much smaller region, with 239 and 610 galaxies in the V and R bands respectively. The X-ray analysis is based on an image obtained with the ROSAT PSPC.

Besides Abell 496 itself, the velocity distribution along the line of sight shows the existence of at least four structures at different redshifts, one of them seeming to be a poor cluster at a velocity of 30083 km/s. The other of these structures have a too large spatial extent to be clusters but may be filaments along the line of sight or other young structures.

Various independent methods show that Abell 496 appears to be a quite relaxed cluster, except perhaps for the distribution of emission line galaxies. These appear to be distributed in two samples falling on to the main cluster, one from the back (the ELGs concentrated towards the west) and one from the front (the high velocity ELGs).

The bright part of the galaxy luminosity function, built from the redshift catalogue, shows a flattening at $R \sim 16$ ($M_R \sim -20.5$), and can be accounted for by a gaussian distribution of bright galaxies and a power law or Schechter function for faint galaxies. The deeper galaxy counts derived from CCD imaging show a dip at $R \sim 19.5$ ($M_R \sim -17$) which can be modelled assuming a cut-off in the luminosity function such as that observed in Coma.

We propose a model for the X-ray gas and derive the galaxy, X-ray gas and total dynamical masses, as well as the baryon fraction in the cluster. Abell 496 appears as a relaxed cluster which can be used as a prototype for further studies.

Key words: Galaxies: clusters: individual: Abell 496; galaxies: clusters of

1. Introduction

In the framework of hierarchical clustering, the Universe is believed to be made of galaxies distributed in sheets encircling voids or filaments, at the intersection of which clusters of galaxies are located. Such models can be tested through the analysis of clusters, which are likely to keep a "memory" of their formation. This is suggested for example by the alignment effects observed in some clusters, such as for example Abell 3558 (Dantas et al. 1997) or Abell 85 (Durret et al. 1998), where the cD, the brightest galaxies, the X-ray emitting gas and possibly even larger scale structures (in the case of Abell 85) all appear aligned along the same direction. Multi-wavelength studies of clusters of galaxies also allow us to draw a global and coherent portrait of these objects, which we can then use to address other questions of interest, such as the influence of mergers and environmental effects at various scales on the properties of both galaxies and X-ray gas. Large scale (i.e. cluster size) mergers are quite often observed from substructures detected in the X-ray gas; smaller scale mergers (i.e. group size) such as the infall of dwarf galaxies onto groups surrounding bright galaxies can be derived from various methods such as those of Serna & Gerbal (1996) or Gurzadyan & Mazure (1998), which require optical velocity and magnitude catalogues; the existence of subclustering also has an influence on the shape of the galaxy luminosity function, which in some cases appears to show a deficit of faint galaxies often interpreted as due to accretion of dwarf galaxies onto larger galaxies or groups (e.g. in Coma, Lobo et al. 1997, Adami et al. 2000). It therefore appears important to analyze cluster properties in detail before using them in other studies. Note in particular that the existence of substructures can lead to overesti-

Send offprint requests to: F. Durret, durret@iap.fr

* Based on observations collected at the European Southern Observatory, La Silla, Chile

mate cluster velocity dispersions, and hence M/L ratios and the value of Ω_0 in clusters.

With the improvement of both observational means (better X-ray detectors, optical multi-object spectroscopy) and modern methods of analysis (some of which are described below), an ever increasing number of clusters showing evidence for merging and environmental effects has been found. A rather general picture has therefore emerged for clusters, with a main relaxed body on to which groups of various sizes can be falling.

Our approach these last years has been to study a small sample of nearby clusters in detail. These have the advantage of being bright, and can therefore be observed in detail within a reasonable amount of telescope time. Besides, they are free of evolution effects. We present here a detailed multi-wavelength study of Abell 496, based on optical (extensive redshift and photometric catalogues) and X-ray (ROSAT PSPC) data.

Abell 496 is a richness class 1 (Abell 1958) cD type (Struble & Rood 1987) cluster at a redshift of 0.0331. For a Hubble constant $H_0=50 \text{ km s}^{-1} \text{ Mpc}^{-1}$, the corresponding scale is 55.0 kpc/arcmin and the distance modulus is 36.52. At optical wavelengths, an adaptive kernel map of the central region (in a $60 \times 60 \text{ arcmin}^2$ square) has revealed a somewhat complicated structure, with a strong concentration of galaxies in the north-south direction (Kriessler & Beers 1997). Note however that this map does not include redshift information. Thorough investigations of the X-ray properties of Abell 496 can be found in Mohr et al. (1999) and Markevitch et al. (1999); their results will be compared to ours in section 4.5.

The paper is organized as follows: we present the data in section 2; the structures along the line of sight derived from the velocity catalogue are described in section 3; the optical properties of the Abell 496 cluster itself are described in section 4; the X-ray cluster properties are described in section 5; a summary and conclusions are given in section 6.

2. The data

2.1. Optical data

Our redshift catalogue includes 466 galaxies in the direction of the cluster Abell 496, in a region covering about $160 \times 160 \text{ arcmin}^2$ ($9.2 \times 9.2 \text{ Mpc}$ for an average redshift for Abell 496 of 0.0331). It is fully described in Durret et al. (1999b).

Our photometric catalogues are described in Slezak et al. (1999). The photographic plate catalogue was obtained by scanning an SRC plate in the b_J band with the MAMA measuring machine at the Observatoire de Paris; it includes 3879 galaxies located in a region of roughly $\pm 1.3^\circ$ from the cluster centre. Positions are very accurate in this catalogue and were used for spectroscopy; on the other hand, b_J magnitudes are not accurate, so a CCD photometric catalogue was obtained in the V and R bands in

order to recalibrate photographic plate magnitudes. The R magnitudes thus estimated for the photographic plate catalogue were used to estimate the completeness of our redshift catalogue. The CCD imaging catalogue includes 239 and 610 galaxies in the V and R bands respectively, and is limited to a much smaller region of $\sim 246 \text{ arcmin}^2$ in the centre of the cluster.

The cluster center will be taken to be the position of the cD galaxy, which coincides with the X-ray maximum: $\alpha = 4^h 33^m 38.45^s$, $\delta = -13^\circ 15' 49.5''$ (2000.0).

2.2. X-ray data

The ROSAT PSPC image (#800024) was taken from the archive and analyzed by Pislar (1998). The cluster was observed during 8972 s. The effective exposure time for this image, after data reduction is 5354 s. We have used the routines developed by Snowden (1995) to obtain a non cosmic background subtracted image between 0.5 and 2 keV. We have defined the image limiting radius ($\sim 1620 h_{50}^{-1} \text{ kpc}$) as the radius where the surface brightness reaches the surface brightness of the cosmic background ($3 \cdot 10^{-4} \text{ s}^{-1} \text{ arcmin}^{-2}$). The different PSPC background components are detailed in Snowden et al. (1994).

The global X-ray gas temperatures derived from Einstein and EXOSAT satellite data are $3.9 \pm 0.2 \text{ keV}$ (David et al. 1993) and $4.7_{-0.8}^{+1} \text{ keV}$ respectively (Edge & Stewart 1991).

3. Velocity distribution along the line of sight

We first discuss the overall properties derived from the velocity distribution along the line of sight.

3.1. Overall characteristics of the structures detected along the line of sight

A wavelet reconstruction of the velocity distribution along the line of sight is displayed in Fig. 1 (466 galaxies). We remind the reader that this type of reconstruction takes into account structures at a significance level of at least 3σ , and detects structures at various scales. The sample was analyzed with 256 points, and the smallest scale was excluded because it is very noisy. A more detailed description of this technique can be found in Fadda et al. (1998).

Nine “groups” or velocity substructures are found with this method, and their velocity characteristics are given in Table 1. The group number is given in col. 1, the number of galaxies in col. 2, the BWT mean velocity (Beers et al. 1990) and corresponding BWT velocity dispersion in cols. 3 and 4, and the velocity interval in col. 5. Foreground groups 1 and 2 and background groups 7 and 8 are most probably not real groups, since they are widely spread both on the sky and in velocity distribution; because of the small number of galaxies involved in the first three of these groups, we did not calculate mean veloci-

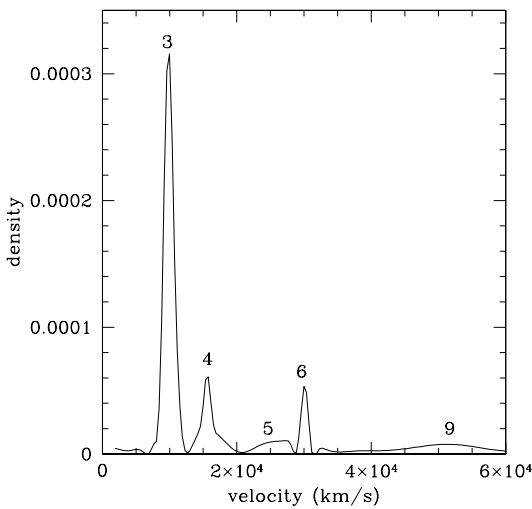


Fig. 1. Wavelet reconstruction of the velocity distribution in the direction of Abell 496. The numbers above the peaks correspond to those of the structures described in the text and in Table 1. The density units correspond to a total integrated galaxy density of 1.

ties or velocity dispersions for these structures. For group 8 these values are only indicative, but characteristic of a low mass structure. Group 3 appears to be the cluster Abell 496 itself. Except for 7 objects, all the galaxies in group 4 appear to be located north of Abell 496. Group 5 has the same kind of shape and size as group 4 and is roughly coaligned with Abell 496 along the line of sight. Group 6 appears strongly concentrated both spatially and in velocity space, all but two galaxies being located west of Abell 496. Moreover, its velocity dispersion is also low.

Table 1. Structures detected along the line of sight

Name	N_{gal}	v_{mean} (km/s)	σ_v (km/s)	velocity interval (km/s)
1	6			[1803,3396]
2	6			[5124,6233]
3	274	9885	715	[7813,11860]
4	59	15758	1214	[13458,17928]
5	25	25361	1627	[23477,28209]
6	29	30083	380	[29144,30814]
7	5			[40606,41650]
8	9	46349	263	[45836,46660]
9	22	52358	1467	[50052,54727]

These results are confirmed when we apply the same method as for the ENACS clusters (Katgert et al. 1996, Mazure et al. 1996) to detect velocity structures along the line of sight. This method consists in sorting the galaxies in order of increasing velocity, and plotting their rank as a function of velocity (hereafter the rank-velocity classification). If the distribution of galaxies in redshift space is

strictly gaussian, we expect to see a regular S-shape in the sequence/gap space. When there are more than 5 galaxies between two successive gaps, we consider that the galaxies belong to a structure.

3.2. A finer analysis of structures 4, 5, 6 and 9

In order to understand whether groups 4, 5, 6 and 9 can be physically coherent structures, we performed a Serna & Gerbal (1996) analysis for each of these groups separately. Since this type of analysis takes into account galaxy magnitudes, we had to eliminate one galaxy in group 4 and one in group 5, for which we have no magnitude in our redshift catalogue. We also tried keeping these galaxies and assigning them an “average” magnitude $R=17$. The results in both cases were similar. Note that the redshift catalogue completeness is about 50% in regions 4 and 5, and 55% in region 9, within the magnitude limit $R=18.8$. It could therefore be argued that the Serna & Gerbal method is meaningless for these samples. However, in this type of analysis it is the brightest galaxies which mainly contribute to the dynamics of the system (since the mass to luminosity ratio is taken to be constant for all galaxies). If the samples are limited to magnitudes $R \leq 17.0$, the redshift catalogue completeness then becomes 72%, 72% and 79% for regions 4, 5 and 9 respectively, and the Serna & Gerbal method is therefore fully applicable.

Table 2. Substructures detected along the line of sight

Name	N_{gal}	v_{mean} (km/s)	σ_v (km/s)
4a	9	14043	381
4b	10	17568	243
4c	9	15302	201
4d	9	15604	131
5a	4	23785	195
5b	4	25159	174
5c	5	26719	457
9a	6	54164	119
9b	5	51165	28
9c	8	52013	348

The characteristics of the substructures found with the Serna & Gerbal method are given in Table 2. Structure 4 has subgroups 4c and 4d well defined in space; they extend over 5 and 3.6 Mpc respectively and could therefore be members of two different clusters. Due to their large spatial extent, subgroups 4a and 4b respectively seem to be just forward and background galaxies, with the exception of the five galaxies of group 4a at the north west extremity (see Fig. 2).

Subgroups 5a and 5b form structures with a small velocity dispersion, but extending over about 7 Mpc, a size which appears rather large for these groups to be members

of two background clusters; the extent and the velocity dispersion of 5c are even larger (Fig. 2).

While the Serna & Gerbal (1996) method finds dynamical sub-structures for the other groups along the line of sight, the same method reveals no substructures in group 6, except for two pairs of galaxies; group 6 therefore appears well defined both in velocity distribution and in space. Eighteen galaxies are included in an ellipse with a major and minor axes of about 8 and 3 Mpc, suggesting that this is a poor, diffuse and low mass cluster (Fig. 2).

Finally, three subgroups are apparently found in structure 9, 9a and 9b having very small velocity dispersions but spanning a rather large spatial region. The overall velocity field in group 9 shows an interesting pattern looking like a velocity gradient (Fig. 3). This could be a filament more or less aligned along the line of sight.

A rank-velocity classification applied to each group confirms that group 4 and possibly group 9 appear to have three substructures (two clear breaks in the curves), group 5 has three or four substructures and group 6 has no clear substructure except perhaps for the two or three first galaxies which are probably infalling objects.

To summarize, groups 4 and 9 clearly appear as filaments or at least elongated structures along the line of sight, but not really massive clusters. This analysis is confirmed by the iso-velocity contours of group 9. The continuous velocity gradient could be interpreted as the result of a merger, with the infalling groups not perfectly aligned along the line of sight. Group 6 has a low velocity dispersion and is probably a poor cluster. Group 5 exhibits two low velocity dispersion sub-structures and a moderately high velocity dispersion group (5c), but the number of galaxies in 5c is too low to provide a robust estimation and we assume that this structure is not a cluster.

We will now discuss the dynamical state of the main structure on the line of sight: the cluster Abell 496 itself (group 3).

4. Morphological and physical properties of Abell 496

4.1. Morphology of the cluster at various wavelengths

We display in Fig. 4 the superposition of the optical image of the cluster with ROSAT PSPC X-ray and radio isocontours. The X-ray contours are quite smooth, with no obvious substructures. However, there appears to be an excess of X-ray emission towards the north west, in the direction where there is also an excess of emission line galaxies (see below). A radio source is visible south east of the cluster, probably associated with a galaxy.

4.2. The galaxy velocity distribution in Abell 496

The cluster Abell 496 corresponds to structure 3 in Table 1; it has a BWT mean velocity of 9885 km/s and a global

velocity dispersion of 715 km/s. The corresponding velocity interval is [7813,11860 km/s] and includes 274 galaxies. Note that the cD galaxy has a velocity of 9831 km/s, close to the mean cluster velocity, and is located very close to the X-ray emission center, suggesting that the cD is at the bottom of the cluster gravitational potential well. This is an indication of a quiescent history of the cluster (see e.g. Zabludoff et al. 1993, Oegerle & Hill 1994).

The wavelet reconstruction of the velocity distribution of Abell 496 shown in Fig. 5 (274 galaxies) suggests the presence of a certain amount of substructure. The sample was analyzed with 256 points, and the two smallest scales were excluded. The corresponding velocity distribution is non-gaussian; it shows: a tiny feature at \sim 8300 km/s; a main asymmetric peak in the [8500, 10700 km/s] range containing 232 galaxies, with a BWT mean velocity of 9769 km/s, and a BWT velocity dispersion of 518 km/s; note that this velocity structure is not quite centered on the velocity of the cD galaxy; a smaller peak at 10940 km/s with 36 galaxies in the [10700, 11860 km/s] range. If we only keep the largest scales, we are left with a rather symmetric velocity distribution showing an excess at high velocities. This excess corresponds to the peak at 10940 km/s, which contains a small number of galaxies (see section 4.4).

These structures are also found by applying a rank-velocity classification, which gives two breaks globally consistent with those found by analyzing the cluster velocity distribution. Such breaks probably indicate substructures with velocities coherent with the finer analysis based on the wavelet technique. However, the number of galaxies involved in these structures is small, and the velocity distribution in the main cluster therefore appears to be quite smooth, suggesting that Abell 496 is quite well relaxed.

In order to confirm the state of relaxation of Abell 496, we have applied a Serna & Gerbal (1996) analysis to the subsample of 96 galaxies located within a radius of 1800 arcsec around the cD and with magnitudes $R \leq 17.0$; within this limited sample, the completeness of the redshift catalogue is 82% and this type of analysis is expected to give robust results. Note that galaxies in this region with measured velocities but without published magnitudes were discarded. Results are displayed in Fig. 6. At the extreme lower right of the figure, we can see the very tight pair made by the cD (#280, $R=12.2$) and a satellite galaxy (#292, $R=15.6$, in the Durret et al. 1999b catalogue): this confirms that the cD is at the bottom of the cluster potential well. We also observe a structure of 11 bright galaxies (10 galaxies with $R \leq 15.8$, plus one with $R=16.8$) highly concentrated in space around the cD (mean distance to the cD: 216 arcsec, with a dispersion of 48 arcsec) but not in velocity (BWT mean velocity and velocity dispersion: 9745 and 375 km/s). This result is comparable to what is found in other clusters, where the central core is more or less well discriminated. The main body of the cluster center appears quite relaxed, with no strong subclustering

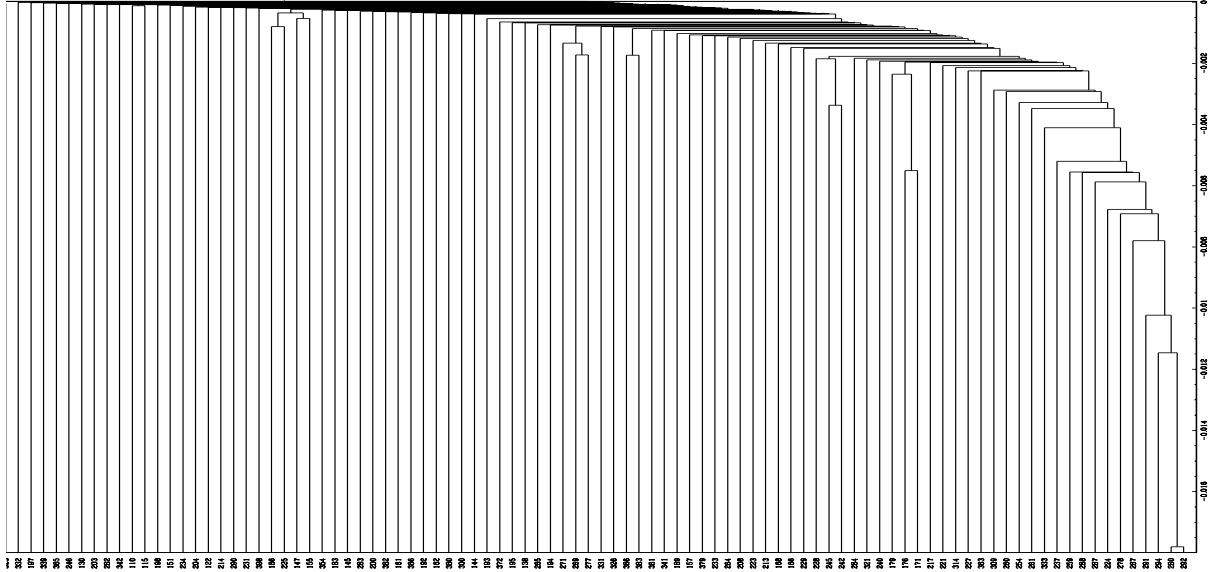


Fig. 6. Dendrogram obtained by applying a Serna & Gerbal analysis to the subsample of 96 galaxies located within a radius of 1800 arcsec around the cD and with magnitudes $R \leq 17.0$. The small numbers at the bottom correspond to the galaxy numbers in our velocity catalogue.

within a radius of 1800 arcsec (1.65 Mpc). This picture agrees with the general shape of Abell 496 seen in X-rays (see Fig. 4).

4.3. Luminosity segregation in Abell 496

After violent relaxation, two-body gravitational interactions lead to a certain level of energy equipartition between galaxies of various masses, and consequently to a certain segregation in velocity dispersion with luminosity (mass). This process concerns essentially massive galaxies, and added to dynamical friction, it creates segregation with distance to the cluster center. The stage of post-violent relaxation therefore leads to a segregation in the $[L, \sigma_v]$ space larger in the central regions than in the overall cluster.

In order to search for such effects in Abell 496, we have derived the velocity dispersion and the average distance of galaxies to the cluster center (defined by the position of the cD) in several magnitude bins. We restrict our sample to galaxies belonging to the cluster, i.e. in the velocity range [7813, 11860 km/s], and within 1000 and 1800 arcsec from the cluster center, in order to have reasonably complete samples: 100% and 79% complete for $R \leq 18.5$ respectively. The completeness is estimated by comparing the number of galaxies with measured redshifts to the number of galaxies in our photographic plate catalogue, for the same R magnitude limit. Since there are 2 galaxies with $R < 14$ and 6 with $14 < R < 15$, we chose to fit the data with two different “brightest” bins: one including the 8 galaxies with $12 < R < 15$, and the other including only the 6 galaxies with $14 < R < 15$.

The velocity dispersions estimated in several magnitude bins are different for the two samples, as shown in Fig. 7. In a 1000 arcsec radius, the velocity dispersion increases more steeply with magnitude: the corresponding slopes are 65 ± 43 and 70 ± 50 $\text{km s}^{-1} \text{mag}^{-1}$ when the brightest bin is included or not respectively. In a 1800 arcsec radius, the velocity dispersion increases less with magnitude, the corresponding slopes being 52 ± 30 and 32 ± 41 $\text{km s}^{-1} \text{mag}^{-1}$.

As seen in Fig. 8, the average distance to the cluster center is somewhat smaller for the galaxies located in the brightest bin ($R \leq 15$), then remains roughly constant with a possible decrease with increasing magnitude, specially in the broadest sample (1800 arcsec radius).

The combination of Figs. 7 and 8 seems to correspond well to a post-violent relaxation stage.

Interestingly, we can notice that both the distance to the cluster center and the overall velocity dispersion range are reduced when emission line galaxies (hereafter ELGs) are excluded. This agrees with the general scheme that ELGs are often found in the outskirts of clusters of clusters and are not as strongly tied to the cluster gravitationally (e.g. Biviano et al. 1997). We now discuss in more detail the properties of ELGs in Abell 496.

4.4. The emission line galaxy distribution

We now compare the distribution of emission line (ELGs) versus non-emission line (NoELGs) galaxies. There are 85 ELGs and 381 NoELGs in our velocity catalogue, among which 34 ELGs and 241 NoELGs in the velocity range of Abell 496. The global percentage of ELGs in the cluster is

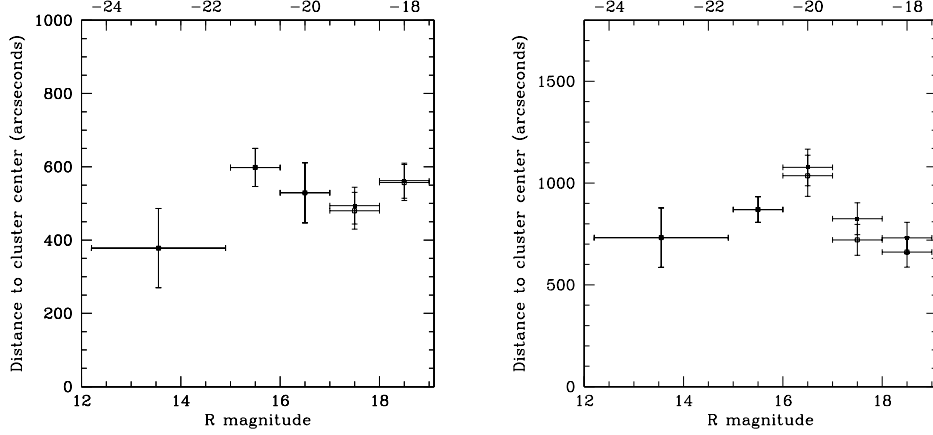


Fig. 8. Average distance to the cluster center for several magnitude bins. The sample is restricted to galaxies in the velocity range [7813,11860 km/s], within 1000 arcsec (left) and 1800 arcsec (right) from the cluster center. Filled squares include all galaxies, empty squares indicate non-emission line galaxies.

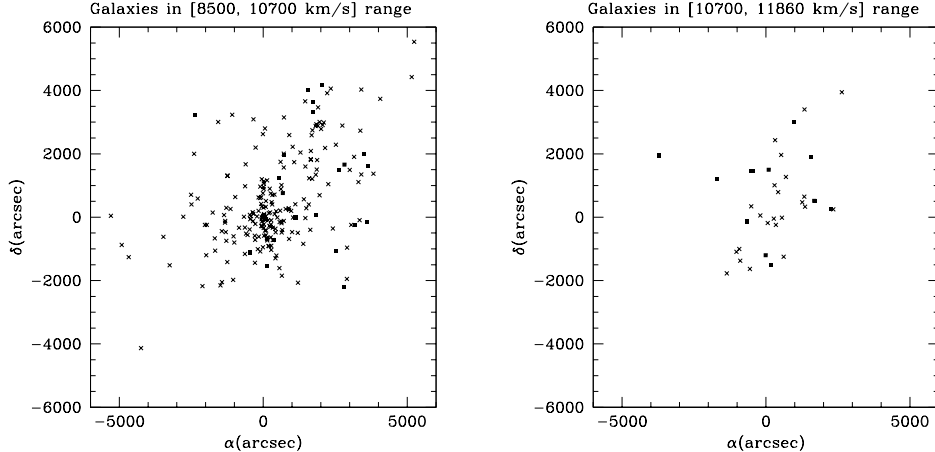


Fig. 9. Left: positions of the 211 non-emission line galaxies (crosses) and of the 21 emission line galaxies (filled squares) in the [8500, 10700 km/s] velocity range. Right: positions of the 23 non-emission line galaxies (crosses) and of the 13 emission line galaxies (filled squares) in the [10700, 11860 km/s] velocity range.

therefore $\sim 12 \pm 3\%$. Note that this percentage is perfectly coherent with the proportions observed by Biviano et al. (1997) in the ENACS survey.

The spatial distribution of the 211 NoELGs and 21 ELGs belonging to the main [8500, 10700 km/s] velocity peak is displayed in Fig. 9. The fraction of ELGs in this velocity range is $9 \pm 3\%$, consistent with the global cluster value within the error bars. NoELGs appear rather homogeneously distributed, except for a sort of linear north-south concentration towards the center. On the other hand, a large majority of the ELGs in this velocity range is located west of a north to south line crossing the center, and at least half of these ELGs even seem to be close to the west cluster edge. This agrees with the fact that ELGs tend to concentrate in the outer regions of clusters (see e.g. results based on ENACS data by Biviano et al. 1997). The presence of an excess of ELGs can at least in some cases be interpreted as due to merging events

producing shocks which trigger star formation. This was shown to be the case in the zone of Abell 85 where the X-ray filament merges into the main body of the cluster (Durret et al. 1998): an excess of ELGs was observed in that region, together with a temperature increase of the X-ray gas. The ASCA X-ray gas temperature map presently available for Abell 496 (Markevitch et al. 1999, Donnelly, private communication), does not show any temperature increase for the X-ray gas in that area, so we cannot correlate the excess of ELGs towards the west cluster edge with a higher gas temperature zone. However, we can note that this excess is located roughly in the same region as the X-ray excess emission in the north west region of the cluster (Fig. 4). Such an X-ray enhancement could be due to a merging event originating from the north west, but our data cannot show this with certainty.

On the other hand, the spatial distributions of the 23 NoELGs and 13 ELGs in the [10700, 11860 km/s] velocity

interval are comparable (Fig. 9), while the ELG fraction seems much higher: $36 \pm 18\%$. Though the small number of objects may introduce errors, there definitely seems to be an excess of ELGs with somewhat higher velocities than the bulk of the cluster; these ELGs account at least partly for the peak at 10940 km s^{-1} in the wavelet reconstruction of the velocity distribution.

A general picture for the ELG distribution in Abell 496 is that of two samples of galaxies falling on to the main cluster, one from the back (the ELGs concentrated towards the west) and one from the front (the high velocity ELGs).

4.5. The galaxy luminosity function

We have seen in the previous section that Abell 496 appears to have properties common to many clusters, with a relaxed main body and ELGs probably falling on to the cluster. We therefore expect its galaxy luminosity function not to be strongly modified by environmental effects, as observed in some clusters showing more prominent sub-structures. We discuss below its main features.

4.5.1. The bright end of the galaxy luminosity function

We have first derived the galaxy luminosity function (GLF) of Abell 496 in the R band from the redshift catalogue, within a radius of 1800 arcsec around the center, and for a limiting magnitude $R=18.5$. There are 196 galaxies in this sample. The completeness of the redshift catalogue within these limits is 79%, and it is 100% in that region for $R \leq 16.0$. The obvious interest of such a GLF is that no background contribution needs to be subtracted, therefore making the results very robust. We have limited the magnitude interval to the [13,18.5] range, because for $R \leq 13$ there is only one galaxy (the cD), which introduces edge effects in the wavelet reconstruction of the GLF, and for $R \geq 18.5$ the completeness sharply decreases. This corresponds to the $[-23.5, -18.0]$ interval in R absolute magnitude.

The GLF obtained after a wavelet reconstruction is shown in Fig. 10. The sample was analyzed with 128 points, excluding the two smallest scales. The significance level of the detected features is at least 3σ . A flattening is observed at $R \sim 16$, corresponding to an absolute magnitude $M_R \sim -20.5$. This shape is comparable to that found in Virgo (Binggeli et al. 1988) and in Abell 963 (Driver et al. 1994), where a comparable flattening was observed at a common absolute magnitude of -19.8 . The GLFs of Coma and Abell 85 are more complex, with a “bump” corresponding to the brightest galaxies, followed by a “dip” at $M_R \sim -20.5$ (see Fig. 9 in Durret et al. 1999a). Note that the flattening of the GLF in Abell 496 occurs exactly at the same absolute magnitude as the dip in Abell 85 and Coma.

The GLF in Abell 496 suggests at least a bimodal galaxy distribution, with bright (mostly elliptical) galaxies in the bright part and dwarf galaxies in the fainter part. We therefore performed a fit of the wavelet reconstructed GLF of Abell 496 by summing two functions: a gaussian, to account for bright galaxies, and a power law (case 1) or a Schechter function (case 2) to represent faint and/or dwarf galaxies. In case 1, we fit the data as a function of apparent R magnitude; the gaussian is then found to be centered on $R=15.19 \pm 0.01$, with $\sigma = 0.8 \pm 0.1$, and the power law varies as $R^{11.67 \pm 0.16}$. In case 2, we fit the data as a function of absolute R magnitude, to allow a direct comparison with other authors; the gaussian is then found to be a little broader, centered on $R=15.48 \pm 0.04$, with $\sigma = 1.0 \pm 0.1$; the Schechter function, defined as in Rauzy et al. (1988, section 3.2.3), has $\alpha = -1.19 \pm 0.04$ and $M_* = -19.43 \pm 0.13$ (in the $[-23.5, -18.0]$ absolute magnitude range).

The GLF resulting from these various fits is shown in Fig. 10; it obviously reproduces the data very well. Except at the faint end where the sample incompleteness most probably modifies the GLF shape, both fits 1 and 2 are good but we cannot distinguish between them. In view of the obvious quality of the fit, we did not attempt to estimate error bars with Monte-Carlo simulations, as done previously e.g. for Abell 85 (see Durret et al. 1999a, Fig. 12).

The various values obtained from these fits of the GLF can be compared to those found in other clusters. The gaussian used to fit the bright part of the GLF in Abell 85 has $\sigma = 1.1$, comparable to the value we find in case 1. The Schechter function for Abell 496 has a slope comparable to that found by Lumsden et al. (1997), but notably flatter than the values found in other surveys (e.g. Valotto et al. 1997, Rauzy et al. 1998 and references therein). Rauzy et al. (1998) argued that the flatter slope found by Lumsden was due to incompleteness at faint magnitudes; this may also be true in our case, since our sample is 100% complete only to $R=16.0$ ($M_R = -20.5$), and we also find a brighter value of M_* than the above surveys, suggesting that we are missing faint galaxies.

We can note that the GLFs of Coma and Abell 85 were interpreted in a similar way, with the bright part mainly due to ellipticals (with a small contribution of spirals) and the faint part due to dwarfs (Durret et al. 1999a). Comparable shapes were found in several other clusters. The fact that the GLF of Abell 496 shows a flattening at the same value $M_R = -20.5$ indicates that the galaxy population in Abell 496 is comparable to those of the above mentioned clusters.

Note that Molinari et al. (1998) have analyzed the GLF of Abell 496 from a photometric catalogue in three colors, reaching magnitudes much fainter than those of our spectroscopic catalogue. We will therefore compare our results to theirs in the next section.

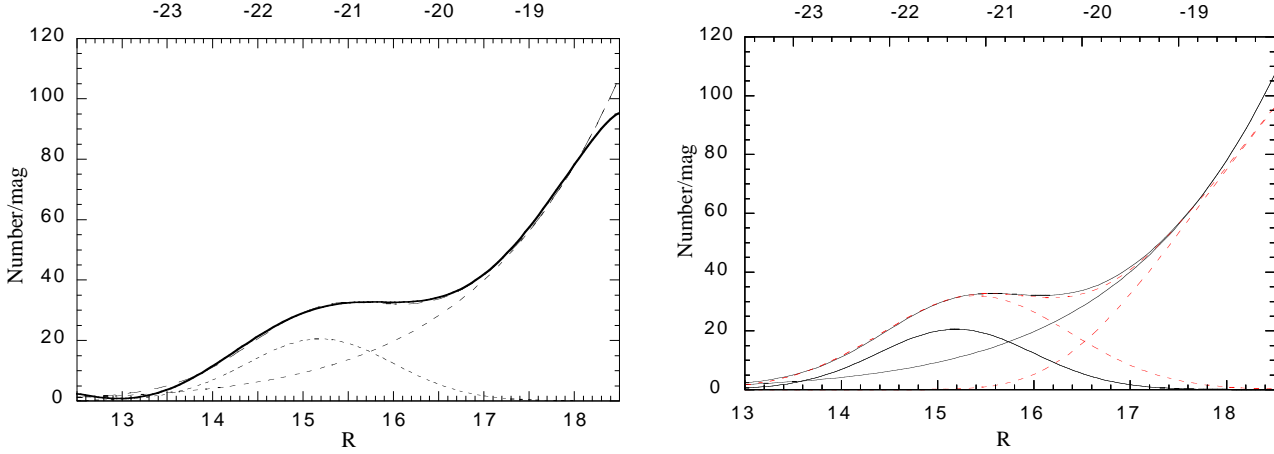


Fig. 10. Left: wavelet reconstruction of the luminosity function in the R band for the 196 galaxies in the redshift catalogue with velocities in the cluster range, within a radius of 1800 arcsec and a limiting magnitude $R=18.5$ (full line). The contribution of the bright and faint populations accounted for by a gaussian and a power law respectively are also shown (dots and short dashes), as well as their sum (long dashes). The top scale indicates R absolute magnitudes. Right: contributions of the bright and faint populations accounted for by a gaussian and a power law (full line), and by a gaussian and a Schechter function (dashes). The sums of both functions are also displayed.

4.5.2. The faint end of the galaxy luminosity function

Our intent was also to derive the luminosity function from the CCD catalogue, which corresponds to a small region of ~ 246 arcmin 2 in the cluster center. For this we first performed a wavelet reconstruction of the R magnitude distribution in the R magnitude range [17,23]. Since we have no background exposure, we estimated the background contribution by connecting the counts from the Las Campanas Redshift Survey (LCRS, Lin et al. 1996) and from the ESO-Sculptor Survey (ESS, Arnouts et al. 1997), as described in our study of Abell 85 (Durret et al. 1999a, Fig. 10 and text), and we subtracted this background to the observed number of galaxies. The result is shown in Fig. 11. We have checked that the consistency of the background number counts estimated by Tyson (1988) with those of the LCRS and ESS combined as described above is good.

The difference between the observed number of galaxies and the background (Fig. 11) becomes negative for magnitudes $R \geq 18.4$, while the CCD catalogue is complete at least up to $R=21$. Therefore, this background cannot be considered as representative of the local background in our CCD field of view. Note that this was already the case for the CCD photometric data of Abell 85.

One notable feature is the dip in the galaxy magnitude distribution at $R \sim 19.5$ ($M_R \sim -17$), which is detected at a high confidence level. This dip corresponds to that observed by Molinari et al. (1998), who found a dip at $R \sim 19$ ($M_R \sim -17.5$). Note that they also find a similar dip in the g band, and possibly in the i band. Molinari et al. (1998) made a second determination of the GLF by selecting cluster members in a colour-magnitude diagram. In this case, they find a small dip, or at least a

flattening, for $R \sim 18$ ($M_R \sim -18.5$). This value does not agree either with the bright nor with the faint GLF that we derived. It is difficult to understand why, since their colour-magnitude relation appears quite well defined.

In order to investigate the origin of the dip seen in our data, we propose a toy model, which is not a fit but only illustrates how the dip could be accounted for. Let us first note that the contribution of the other structures detected along the line of sight is negligible. Assuming a Gaussian + a Schechter function to model the GLF (see section 4.5.1), we rescaled the number of galaxies produced by this composite function to fit the dimension of the CCD field. We then applied a magnitude cut-off to this GLF, as suggested by Adami et al. (2000), for galaxies fainter than $M_R = -19.75$ in the inner core of the Coma cluster. This effect becomes very strong for galaxies fainter than $M_R = -17$. The exact shape of such a cut-off is unknown, so we applied a convenient apodization function (the choice of this function influences the shape and smoothness of the dip). The background counts were modeled as the background contribution from the LCRS and ESS described above. We then summed the cluster and background contributions, and the result is shown in Fig. 12.

Such a toy model can reproduce the global GLF shape, with counts similar to the observed data and a dip comparable to the observed one. A fine-tuning of the various parameters involved could make Figs. 11 and 12 more similar, but this would push the model too far. However, we can state that a cut-off in the GLF of Abell 496 similar to that observed in Coma is a solution to account for the observed dip.

Table 3. Fits of the X-ray gas with a β -model and a Sérsic model

Model	n_0 (10^{-3} cm $^{-3}$)	β	r_c (kpc)	ϵ	R_{cool} (kpc)	\dot{M} (M_\odot /yr)
1	21.7	0.53	50	0.87	192	235
	1.9	0.01	4	0.03	25	81
2	2.55	0.82	356	0.86		
	0.35	0.07	58	0.03		
Model	I_0 (10^{-3} cm $^{-3}$)	ν	a (kpc)	ϵ	R_{cool} (kpc)	\dot{M} (M_\odot /yr)
3	5.5	0.61	230	0.86	198	314
	0.3	0.02	12	0.03		
4	2.7	0.75	368	0.85		
	1.3	0.17	129	0.03		

Notes to Table 3: n_0 , β and r_c are the parameters of the best β -model fit, and I_0 , ν and a those of the best Sérsic fit; ϵ is the cluster ellipticity, R_{cool} the cooling radius and \dot{M} the cooling flow mass deposit rate.

Models 1 and 2 correspond to a β -model, with the central region respectively included or not; models 3 and 4 correspond to a Sérsic model with the central region respectively included or not. For each model, the first line gives the parameters and the second line the corresponding 3σ errors.

5. The X-ray gas

A pixel by pixel fit was performed on the X-ray image, as described by Pislar et al. (1997). The pixel size is 30 arcsec. A β -model and a 3D Sérsic model (Lima Neto et al. 1999) were considered for the variations of the density with radius. The global temperature estimated from these ROSAT data, using a Raymond-Smith spectrum and a Galactic absorption column density was found to be 4 ± 1 keV and assumed to be constant (Pislar 1998). This is consistent with the temperatures of 3.9 and 4.7 keV previously measured with the Einstein and EXOSAT satellites respectively (David et al. 1993; Edge & Stewart 1991). The parameters corresponding to the best fits for both models are given in Table 3, and the result of the β -model 1 fit superimposed on the observed image is displayed in Fig. 13. We observe that in model 2 the central density is lower than in model 1 and that the β and r_c parameters are higher. This is because in model 2 we do not include the central region, where the cooling flow lies. The effect is the same for models 3 and 4.

Our values of β and r_c (in model 2) are higher than those of Markevitch et al. (1999), who found $\beta = 0.7$ and $r_c = 249$ kpc. This is due to the fact that they exclude a central region smaller than ours (3 arcmin instead of 3.3 arcmin). Pislar (1998) has shown that in a cooling flow cluster the bigger the excluded central region, the higher β and r_c , and the lower the central density. Moreover, at the image limiting radius, the values of the dynamical and gas masses do not depend on the size of the central region excluded.

The cooling radius R_{cool} and the mass \dot{M} deposited in the centre were estimated as in Pislar et al. (1997) and

are given in Table 3 for a temperature of 4 keV. We take $2 \cdot 10^{10}$ yr for the cooling time.

The X-ray gas and total dynamical masses derived from the X-ray data assuming equilibrium are shown in Fig. 14 as a function of radius. Note that these curves are only valid between the cooling radius and the limiting radius of the X-ray image; within this validity range, both models are in good agreement with each other.

We find, with models 2 and 4 for a prolate geometry, at the limiting radius of the image, a gas mass $(6.1 \pm 2.2) \cdot 10^{13} M_\odot$ and a dynamical mass of $(4.2 \pm 1.1) \cdot 10^{14} M_\odot$. We overestimate the errors because we have supposed that the parameters are not correlated. The masses at $1 h_{50}^{-1}$ Mpc are respectively $(3.45 \pm 1.1) \cdot 10^{13} M_\odot$ and $(2.4 \pm 0.6) \cdot 10^{14} M_\odot$. The gas mass found by Mohr et al. (1999) and the dynamical mass found by Markevitch et al. (1999) are very similar if we remember that their geometry is spherical. The mass calculated by the virial theorem applied to all the galaxies in the redshift catalogue with velocities in the cluster is $M_{vir} = (7.2 \pm 0.8) \cdot 10^{14} M_\odot$. This value agrees with the dynamical mass derived above, providing the mass profiles can be extrapolated to radii larger than the X-ray image. The integrated mass of galaxies within the X-ray image limiting radius, assuming a mass to luminosity ratio of $8 M_\odot / L_\odot$, is $1.0 \cdot 10^{13} M_\odot$. Note that, due to incompleteness of our redshift catalogue, in particular at faint magnitudes, this is only a lower limit.

The ratio of the X-ray gas mass to the dynamical mass is shown as a function of radius in Fig. 15. The fraction of X-ray gas is about 0.15 at the limiting radius of the image and at $1 h_{50}^{-1}$ Mpc with a β -model. With a Sérsic model, the ratio is 0.12 at the limiting radius of the image. The baryon fraction that we find at $1 h_{50}^{-1}$ Mpc with the β -model is very similar to that obtained by Markevitch et al. (1999) (0.158 ± 0.017), and comparable to that found in other clusters. At the X-ray limiting radius, the stellar to X-ray gas mass ratio is 16% and the stellar to total dynamical mass ratio is 2.4%.

6. Discussion and conclusions

The optical analysis of the Abell 496 field has shown the existence of several structures along the line of sight. Among these, one (structure 6) is likely to be a poor, diffuse and low mass cluster, while two others (structures 4 and 9) are probably filaments more or less aligned along the line of sight, the latter presenting a smooth velocity gradient. Notice that the distances between these various structures are very large.

The cluster Abell 496 itself has quite a regular morphology. It includes 274 galaxies in the [7813, 11860 km/s] velocity range and has a velocity dispersion of 715 km/s. Its velocity distribution implies a small amount of substructure. The analysis of the correlations between position, luminosity and velocity dispersion indicates a post-violent relaxation state. We can notice that both the dis-

tance to the cluster center and the overall velocity dispersion ranges are reduced when emission line galaxies (hereafter ELGs) are excluded. This agrees with the general scheme that ELGs are often found in the outskirts of clusters and are not as strongly tied to the cluster gravitationally (e.g. Biviano et al. 1997). There may be two samples of ELGs falling on to the main cluster, one from the back (the ELGs concentrated towards the west) and one from the front (the high velocity ELGs).

The bright luminosity function derived from our redshift catalogue shows a flattening at $R \sim 16$ ($M_R \sim -20.5$), comparable to similar shapes found in other clusters. This suggests at least a bimodal distribution, one for ellipticals and one for fainter galaxies. The fact that the flattening occurs at the same absolute magnitude as for other clusters suggests that the galaxy populations in all these clusters are comparable.

At fainter magnitudes, galaxy counts derived from CCD imaging show a dip at $R \sim 19.5$ ($M_R \sim -17$) which can be reproduced if we assume a magnitude cut-off similar to that observed in Coma (Adami et al. 2000). Notice that such a cut-off is observed in the very central regions of both clusters. Although this result is only based on imaging and remains to be confirmed spectroscopically, we may be evidencing a second example of a cut-off of the faint end of the luminosity function in a cluster.

We have modelled the X-ray gas and derived the X-ray gas mass and the dynamical mass, which we compare to the stellar mass. At the limiting radius ($1.62 h_{50}^{-1}$ Mpc) of the image, we find a fraction of X-ray gas to total mass of 0.12–0.15 and a stellar to X-ray gas mass ratio of 0.16. We can note that Abell 496 follows exactly the two by two correlations between the X-ray luminosity ($L_X = 6.8 \cdot 10^{44}$ erg/s, Wu et al. 1999), the X-ray temperature ($T_X = 4$ keV) and the galaxy velocity dispersion ($\sigma_v = 715$ km/s) described in the literature (see e.g. Wu et al. 1999 and references therein). These values are typical of a richness class 1 cluster.

Abell 496 therefore appears to be a relatively quiet and simple cluster, with no strong environmental effects, although we may see an enhancement of the X-ray emission and of the number of emission line galaxies towards the north west.

While Coma has long been the archetype of a relaxed cluster and is not believed to be relaxed any more (see Biviano 1998 and the proceedings of the Coma meeting), the results presented above suggest that Abell 496 may be such a prototype, and can be used as a “template” in the future study of more complex (i.e. substructured) clusters.

Acknowledgements. The authors thank Andrea Biviano for help. C. Adami is grateful to the staff of the Dearborn Observatory for their hospitality during his postdoctoral fellowship. We acknowledge financial support from the French Programme National de Cosmologie, CNRS.

References

Abell G.O. 1958, *ApJS* 3, 211
 Adami C., Ulmer M., Durret F. et al. 2000, *A&A* in press, [astro-ph/9910217](http://arxiv.org/abs/astro-ph/9910217)
 Arnouts S., de Lapparent V., Mathez G. et al. 1997, *A&AS* 124, 163
 Beers T.C., Flynn K., Gebhardt K. 1990, *AJ* 100, 32
 Binggeli B., Sandage A., Tammann G.A. 1988, *ARA&A* 26, 509
 Biviano A., Katgert P., Mazure A. et al. 1997, *A&A* 321, 84
 Biviano A. 1998, Proc. “A new vision of an old cluster: untangling Coma Berenices”, Marseille June 17-20 1997, Eds. Mazure et al., World Scientific, page 1
 Condon J.J., Cotton W.D., Greisen E.W. et al. 1998, *AJ* 115, 1693
 Dantas C.C., de Carvalho R.R., Capelato H.V., Mazure A. 1997, *ApJ* 485, 447
 David L.P., Slyz A., Jones C., et al. 1993, *ApJ* 412, 479
 Driver S.P., Phillipps S., Davies J.I., Morgan I., Disney M.J. 1994, *MNRAS* 268, 393
 Durret F., Forman W., Gerbal D., Jones C., Vikhlinin A. 1998, *A&A* 335, 41
 Durret F., Gerbal D., Lobo C., Pichon C. 1999a, *A&A* 343, 760
 Durret F., Felenbok P., Lobo C., Slezak E. 1999b, *A&AS* 139, 525
 Edge A.C., Stewart G.C. 1991, *MNRAS*, 252, 428
 Fadda D., Slezak E., Bijaoui A. 1998, *A&AS* 127, 335
 Gurzadyan V.G., Mazure A. 1998, *MNRAS* 295, 177
 Katgert P., Mazure A., Perea J. et al. 1996, *A&A* 310, 8
 Kriessler J.R., Beers T.C. 1997, *AJ* 113, 80
 Lima Neto G.B., Gerbal D., Márquez I. 1999, *MNRAS* 309, 481
 Lin H., Kirshner R.P., Schechter S.A. et al. 1996, *ApJ* 464, 60
 Lobo C., Biviano A., Durret F., et al. 1997, *A&A* 317, 385
 Lumsden S.L., Collins C.A., Nichol R.C., Eke V.R., Guzzo L. 1997, *MNRAS* 290, 119
 Markevitch M., Vikhlinin A., Forman W.R., Sarazin C.L. 1999, *ApJ* 527, 545
 Mazure A., Katgert P., den Hartog R. et al. 1996, *A&A* 310, 31
 Mohr J.J., Mathiesen B., Evrard A.E. 1999, *ApJ* 517, 627
 Molinari E., Chincarini G., Moretti A., De Grandi S. 1998, *A&A* 338, 874
 Oegerle W.R., Hill J.M. 1994, *AJ* 107, 857
 Pislar V., Durret F., Gerbal D., Lima Neto G.B., Slezak E. 1997, *A&A* 322, 53
 Pislar V. 1998, PhD Thesis, Université Paris 6
 Rauzy S., Adami C., Mazure A. 1998, *A&A* 337, 31
 Serna A., Gerbal D. 1996, *A&A* 309, 65
 Slezak E., Durret F., Guibert J., Lobo C. 1999, *A&AS* 139, 559
 Snowden S.L. 1995, *Cookbook for analysis procedures for Rosat XRT/PSPC observations of extended objects and diffuse background* (Greenbelt: NASA USRSDC)
 Snowden S.L., McCammon D., Burrows D.N., Mendenhall J.A. 1994, *ApJ* 424, 714
 Struble M.F., Rood H.J. 1987, *ApJS* 63, 543
 Tyson J.A., 1988, *AJ* 96, 1

Valotto C.A., Nicotra M.A., Muriel H., Lambas D.G. 1997,
ApJ 479, 90
Wu X.-P., Xue Y.-J., Fang L.-Z. 1999, ApJ 524, 22
Zabludoff A.I., Geller M.J., Huchra J.P., Vogeley M.S. 1993,
AJ 106, 1273

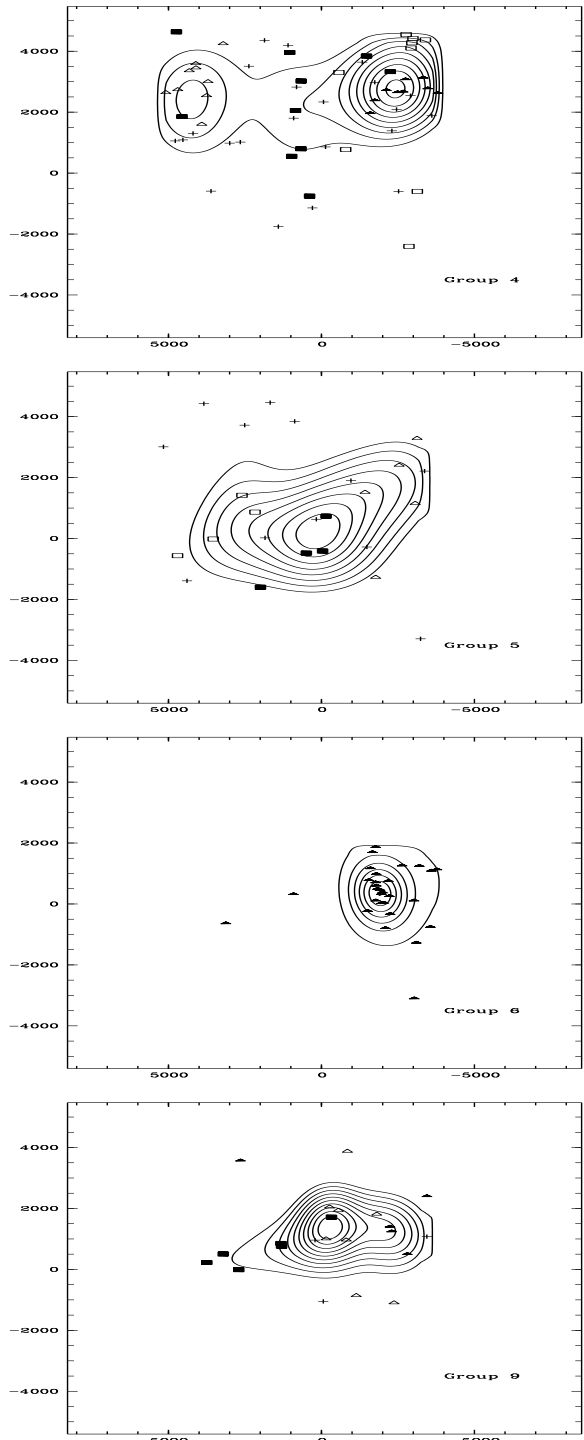


Fig. 2. Isodensity contours for galaxies in structures 4, 5, 6 and 9 (from top to bottom); galaxy positions are superimposed with the following symbols: structure 4: empty rectangles=4a, filled rectangles=4b, empty triangles=4c, filled triangles=4d, crosses=other galaxies in structure 4; structure 5: empty rectangles=5a, filled rectangles=5b, empty triangles=5c, crosses=other galaxies in structure 5; structure 6: all galaxies; structure 9: filled rectangles=9a, filled triangles=9b, empty triangles=9c, crosses=other galaxies in structure 9. Positions are relative to the cluster center defined in the text.

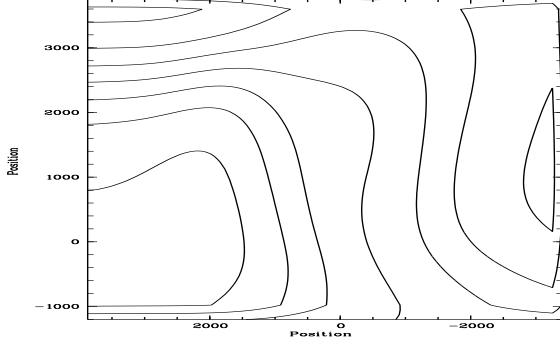


Fig. 3. Isocontours of the velocity field in group 9, from 51000 (right) to 54000 km/s (left) by steps of 500 km/s. Positions are relative to the cluster center defined in the text.

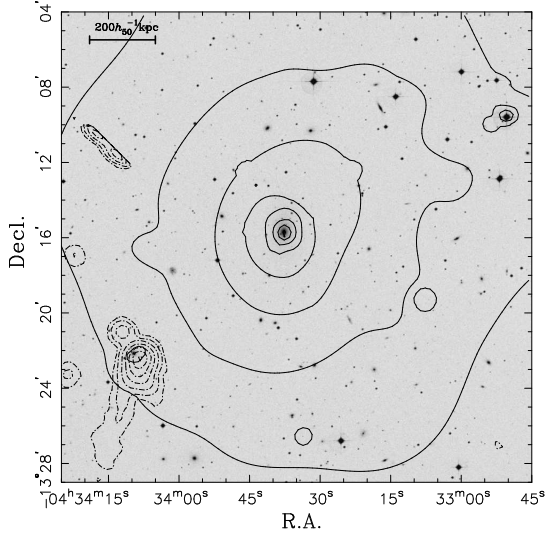


Fig. 4. Optical POSS image of the central region of Abell 496 on to which X-ray (full lines) and radio 1400 MHz (dot-dashed lines) contours are superimposed. The radio data were taken from Condon et al. (1998).

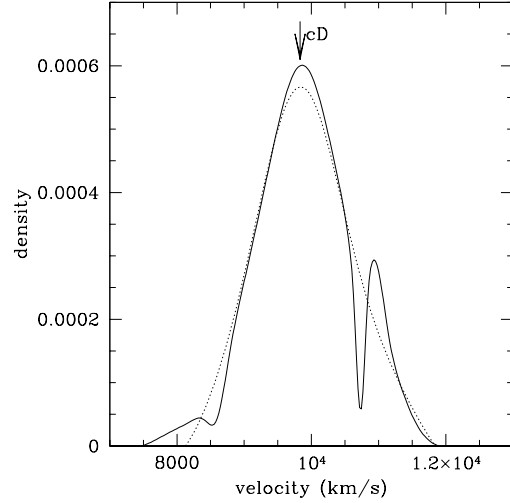


Fig. 5. Wavelet reconstruction of the velocity distribution in the direction of Abell 496, obtained by excluding the two smallest scales (full line) and the three smallest scales (dashed line). The arrow indicates the velocity of the cD galaxy. The density units correspond to a total integrated galaxy density of 1.

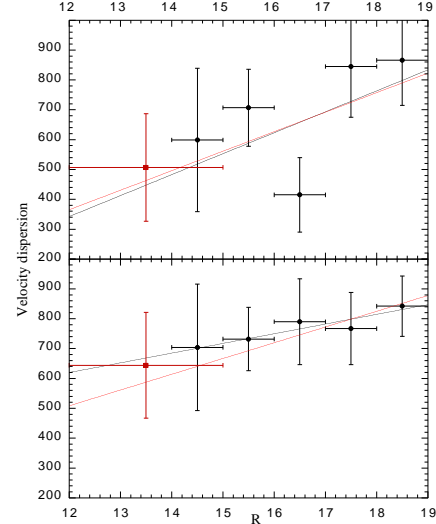


Fig. 7. Velocity dispersion in several magnitude bins. The top figure corresponds to a region of 1000 arcsec radius, the bottom figure to a 1800 arcsec radius. The grey line is the fit including all the points, while the dark line is the fit when the brightest bin is excluded.

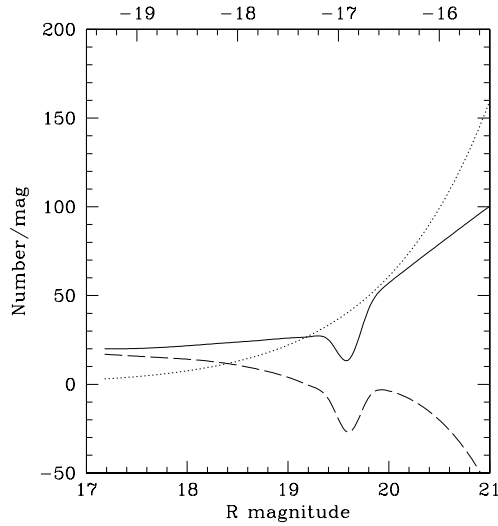


Fig. 11. Wavelet reconstruction of the number of galaxies in the R band for the 411 galaxies in the CCD catalogue within the R magnitude range [17,21] (full line). The background contribution obtained from the LCRS and ESS is shown as a dotted line (see text). The difference between the observed number of galaxies and the background is shown as a long dashed line.

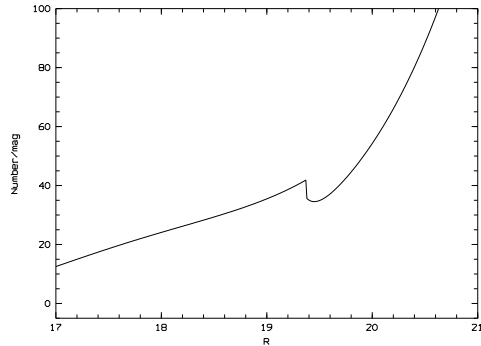


Fig. 12. Model of the total counts reproducing the dip observed in Fig. 11 (see description in text).

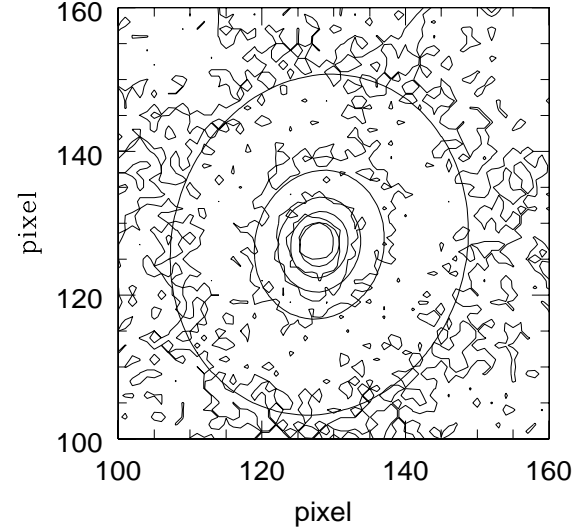


Fig. 13. Observed ROSAT PSPC image with the isocontours of the best β -model fit superimposed (see text). The pixel size is 30 arcsec.

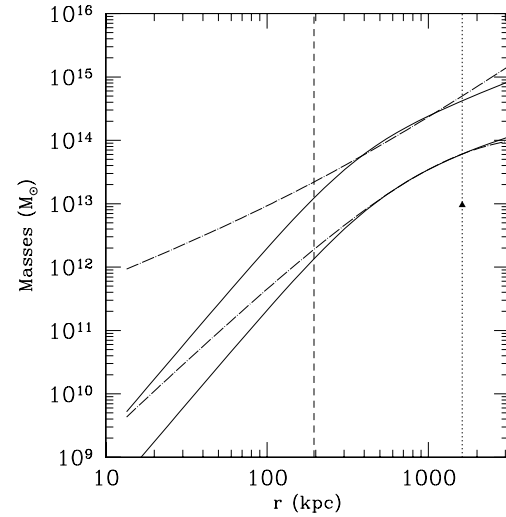


Fig. 14. Masses of the X-ray gas (lower curves) and total dynamical masses (upper curves) derived from the X-ray data. Full lines correspond to β -model fits and dot-dashed lines to Sérsic. The vertical lines indicate the cooling radius (dashes) and the limiting radius of the image (dots). The filled triangle indicates the integrated galaxy mass at the X-ray limiting radius.

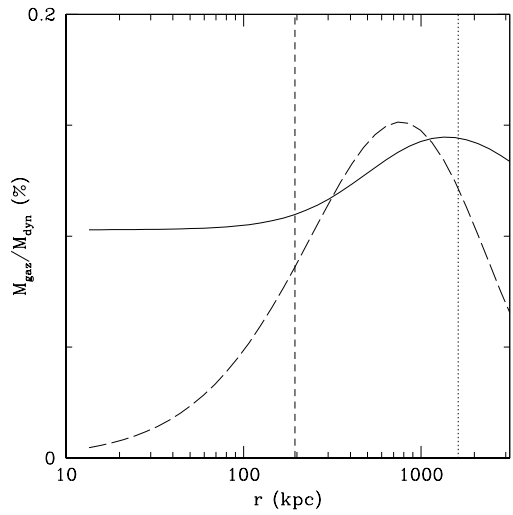


Fig. 15. X-ray gas to dynamical mass ratio. The full line corresponds to the β -model fit and the dot-dashed line to the Sérsic fit. The vertical lines indicate the cooling radius (dashes) and the limiting radius of the image (dots).